Journal of The Electrochemical Society



# Theoretical Insights into Oxidation States of Transition Metals at (001) and (111) $LiNi_{0.5}Mn_{1.5}O_4$ Spinel Surfaces

*Journal of The Electrochemical Society*, **165** (5) A1099-A1103 (2018)
0013-4651/2018/165(5)/A1099/5/$37.00 © The Electrochemical Society


# Theoretical Insights into Oxidation States of Transition Metals at (001) and (111) $LiNi_{0.5}Mn_{1.5}O_4$ Spinel Surfaces

**Nadia N. Intan,** [1] **Konstantin Klyukin,** [1,*] **and Vitaly Alexandrov** [1,2,z]

[1] *Department of Chemical and Biomolecular Engineering, University of Nebraska-Lincoln, Lincoln, Nebraska 68588, USA*
[2] *Nebraska Center for Materials and Nanoscience, University of Nebraska-Lincoln, Lincoln, Nebraska 68588, USA*

Spinel $LiNi_{0.5}Mn_{1.5}O_4$ (LNMO) is a promising cathode material for high energy density lithium-ion batteries (LIBs), but further enhancement of LNMO electrochemical performance requires a better understanding of its intrinsic surface properties. Herein, we employ first-principles calculations to obtain insights into the transition-metal disproportionation reactions and oxidation states at the LNMO (001) and (111) surfaces examining the role of crystal surface, state of charge (lithium content), oxygen vacancies, and protonation of surface oxygen atoms. Our results reveal possible coexistence of multiple transition-metal oxidation states on the (001) facet promoted by surface protonation and presence of oxygen vacancies. This should facilitate Mn dissolution, while it is not the case for the (111) surface.
 [DOI: 10.1149/2.1251805jes]

Manuscript submitted January 30, 2018; revised manuscript received March 21, 2018. Published April 10, 2018.

Spinel-structured lithium manganese oxide $LiMn_2O_4$ (LMO) along with its derivatives is one of the most extensively studied class of cathode materials for rechargeable lithium ion batteries (LIBs).[1–4] Despite some appealing electrochemical properties and low cost, LMO suffers from substantial Mn dissolution causing severe capacity fading and battery degradation.[5–7] It is believed that Mn dissolution stems from the Hunter's disproportionation reaction $2Mn(III) \rightarrow Mn(II) + Mn(IV)$ generating surface Mn(II) species that are prone to dissolution. To alleviate this problem and also increase energy density relative to LMO, mixed spinel oxides such as $LiNi_{0.5}Mn_{1.5}O_4$ (LNMO) were proposed. Cation doping of LMO with divalent Ni species suppresses Mn(III) and stabilizes Mn(IV) states resulting in the redox reactions only at the Ni sites with $Ni^{3+}/Ni^{2+}$ potential of ~4.7 V vs $Li/Li^+$.[8,9] Also, LNMO exhibits no collective Jahn-Teller (JT) distortion as both Ni(II) and Mn(IV) are inactive toward JT distortion and therefore the cubic structure of the material is maintained.[10] Nevertheless, the role of Mn(III) in the electrochemical performance of LNMO is still unclear.[11] While improved, the issue of both Mn and Ni dissolution from LNMO surfaces still remains as significant dissolution of Mn and Ni species has been observed experimentally.[11–14]

A related problem concerns the electrolyte decomposition at the LNMO/electrolyte interfaces at high voltages, and the involvement and dissolution of transition metals toward the overall battery degradations and solid electrolyte interphase (SEI) layer buildup.[15] It was suggested that adsorption of organic electrolyte species on LMO surfaces can assist the reduction of Mn(III) to Mn(II), which leads to Mn dissolution as Mn(II).[16] Interestingly, it was recently observed experimentally for both LMO and LNMO that the amounts of dissolved Mn and Ni increase with the state-of-charge (SOC)[13] and Mn(II) content at LNMO surfaces rises upon battery charging.[18] This is, however, surprising as it contradicts the general belief that Mn(II) appears as a result of the Hunter's disproportionation reaction favored in the discharged state and thus more Mn(IV) is expected upon charging. The authors explained their observations of high Mn(II) content by electrode/electrolyte surface reactions instead of Mn disproportionation reactions.[18] Although it is clear that metal dissolution and electrolyte decomposition are two correlated issues, it is still important to elucidate intrinsic surface properties of LNMO and how they may manifest in the battery degradation process.

It is well recognized that particle morphology and surface terminations can substantially affect electrochemical properties of LMO and LNMO materials.[11,19,20] Previous computational studies provided important insights into the electrode/electrolyte interfacial properties, especially for pure LMO spinel. For instance, surface energies for various surface terminations and reconstructions were computed to predict the equilibrium particle morphologies of both LMO[21,22] and LNMO.[23–25] In the case of LMO, Mn dissolution,[16,26,27] adsorption and decomposition of organic electrolyte molecules[28] at LMO surfaces were also examined. However, little attention has been paid so far to understanding dependencies of transition-metal oxidation states in LNMO on crystal surface, state of charge, the presence of oxygen vacancies and surface protonation by electrolyte species. The present work explores this aspect of LNMO surface chemistry by employing systematic density-functional-theory (DFT) calculations.

## Computational Details

All calculations were performed using the Vienna Ab initio Simulation Package (VASP)[29,30] within the projector augmanted-wave (PAW) approach.[31] The generalized gradient approximation Perdew-Burke-Ernzerhof (GGA-PBE) exchange correlation functional [32] was employed in the modified form for solids PBEsol[33] along with a plane wave cutoff energy of 500 eV. The PAW potentials for Li, Mn, Ni and O contain 3, 13, 10 and 6 valence electrons, respectively. The rotationally invariant Hubbard-type correction was adopted with $U_{eff} = 3.9$ eV and 6.0 eV on the Mn and Ni 3d orbitals, correspondingly. These values were shown to provide a good description of the electronic structure properties for $LiMn_2O_4$ and $LiMn_{1.5}Ni_{0.5}O_4$ .[34–36] Furthermore, we have tested the values of $U_{eff}$ in the range of 3.9 to 4.85 eV for Mn according to previous theoretical studies and found that the choice of $U_{eff}$ value does not affect our conclusions.

It is established experimentally that depending on the synthesis conditions, cubic LNMO spinel can display two different Ni/Mn arrangements: the more energetically favorable ordered $P4_332$ structure and the disordered $Fd\bar{3}m$ structure.[37–39] Our simulations were performed for $LiMn_2O_4$ (space group $Fd\bar{3}m$) and $LiNi_{0.5}Mn_{1.5}O_4$ (space group $P4_332$ ) with ordered distribution of transition-metal cations.

The (001) and (111) surfaces obtained from the fully optimized bulk structure with a vacuum gap of at least 10 Å. A surface cell of $11.71 \times 11.71$ Å$^2$ for $LiMn_2O_4$ and $11.57 \times 11.57$ Å$^2$ were used for $LiMn_2O_4$ and $LiNi_{0.5}Mn_{1.5}O_4$, correspondingly, as shown in Figure 1. When modeling delithiated surfaces we have only considered removal of up to two uppermost Li layers from the slab. All calculations were done with a fully atomic relaxation of the slab until all the forces acting on ions were less than 0.02 eV/Å. For the Brillouin zone sampling of the bulk oxides, we use a $3 \times 3 \times 3$ $k$-point mesh in the Monkhorst-Pack scheme,[40] while a $2 \times 2 \times 1$ $k$-point sampling was used for slabs calculations.

The antiferromagnetic ordering with $\uparrow\uparrow\downarrow\downarrow$ pattern along the (110) direction was adopted in the simulation of LMO, which was reported to be more stable than $\uparrow\downarrow\uparrow\downarrow$ by 4 meV.[22] For Ni-doped $LiNi_{0.5}Mn_{1.5}O_4$ spinel, the antiferromagnetic ordering of $\uparrow\downarrow$ for Ni and Mn was used in accordance with experiments.[41,42] The changes in the net magnetic

*Electrochemical Society Member.
[z]E-mail: valexandrov2@unl.edu

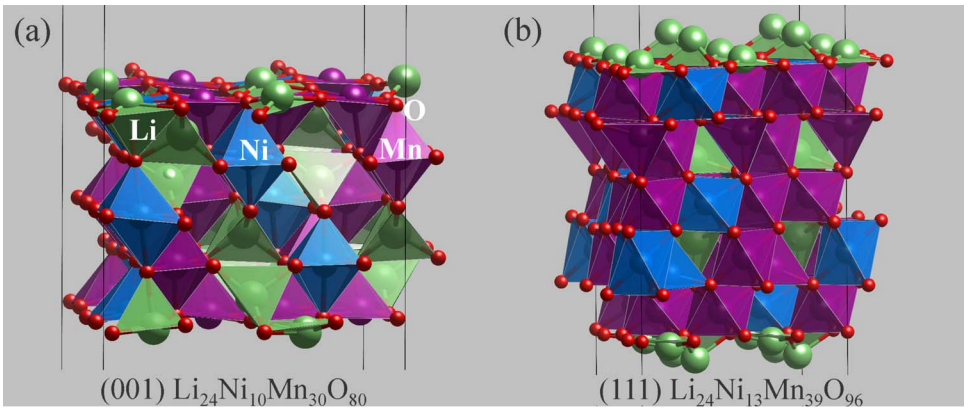


**Figure 1.** Polyhedral representation of symmetric off-stoichiometric slab models for the (001) and (111) surfaces of LNMO used in the present study. Li, Ni, Mn and O atoms are in green, blue, purple, and red, respectively.

moments of both manganese and nickel cations were used to determine their oxidation states. Mn(II), Mn(III) and Mn(IV) oxidation states are determined via net spins of ~4.4 $\mu_B$, ~3.8 $\mu_B$ and ~3.2 $\mu_B$, respectively.[16] The electronic net spins of ~1.6 $\mu_B$, ~0.9 $\mu_B$ were used to differentiate Ni(II) and Ni(III) ions.[17] The most stable distributions of Ni and Mn oxidation states for both LMO and LNMO slabs were confirmed through simulated annealing ab initio molecular dynamics (AIMD) with a 1 fs timestep. An initial 5 ps long AIMD trajectory at 700 K was generated using the Nose-Hoover thermostat followed by gradual cooling at 100K/ps rate. The final structures are optimized at zero Kelvin using static DFT to find the lowest energy configurations. The climbing image nudged elastic band (CI-NEB) method was applied to estimate activation barriers of electron hopping.[43]

## Results and Discussion

It was demonstrated before that LMO and LNMO particles display cubo-octahedral crystal morphology with primarily (111) and (001) surface facets which relative ratio depends on the synthesis conditions such as temperature and oxygen partial pressure.[22] It was also revealed computationally that the most energetically favorable configuration of the (111) surface is the Li-terminated reconstructed (111) facet with no surface transition metals which may partially explain its better resistance to the Mn dissolution.[22] For the stoichiometric slabs of LMO, we estimate the surface energies of 0.75 J/m$^2$ and 0.69 J/m$^2$ for the (001) and reconstructed (111) facets, respectively. In the case of LNMO, the surface energies of the stoichiometric Ni/Mn ordered LNMO phase are computed to be 1.23 J/m$^2$ and 1.25 J/m$^2$ for the (001) and reconstructed (111) surfaces, correspondingly. Note that the reported values for the LMO surface energies in literature vary quite considerably, but our numbers are in good agreement with those previously reported for both LMO[22] and LNMO[24] where similar computational schemes were used. It was also demonstrated on the example of LMO that the surface energies of stoichiometric and off-stoichiometric surfaces are comparable.[22] Overall, the results show that the two surfaces for both LMO and LNMO should exhibit similar stability.

Regarding Mn oxidation states on the (001) LMO surface, we find only Mn(III) ions on the surface for both lithiated and delithiated cases, as shown in Figure 2a. To confirm that Mn(III) are indeed the most favorable cations on the (001) surface, we carry out a series of static DFT and simulated annealing AIMD simulations starting from different initial electronic states. We observe that upon first-layer delithiation some Mn(III) ions in the bulk slab become Mn(IV), but not on the topmost surface. These results are in qualitative agreement with previous theoretical investigation.[44]

It was demonstrated in previous first-principles studies[21,22] that surface reconstruction should play an important role in stabilizing the (111) LMO surface. It was suggested that swapping the Mn cations in the octahedral surface sites with the tetrahedral Li cations in the subsurface leads to a significant surface stabilization. The result of this is the Li-terminated reconstructed (111) LMO surface as shown in Figure 1b in which all surface Mn cations are now fully coordinated by oxygen atoms, while the swapped Mn ions now reside in the tetrahedral sites and have the oxidation state of Mn(II). As there are no under-coordinated Mn cations on the reconstructed surface, we find an equal ratio of Mn(III) and Mn(IV) cations in the topmost MnO layer as in bulk LMO.

For LNMO surfaces, we focus on the energetically more favorable ordered $P4_332$ phase and cleave the surfaces using this Ni/Mn configuration. Ni doping of LMO is supposed to lead to the presence of only Ni(II) and Mn(IV) in LNMO which is the case for LNMO bulk. However, as can be seen in Figure 2b, we find that in the fully lithiated state there is an equal concentration of surface Ni(II) and Ni(III), as well as Mn(III) and Mn(IV). Specifically, we find that different

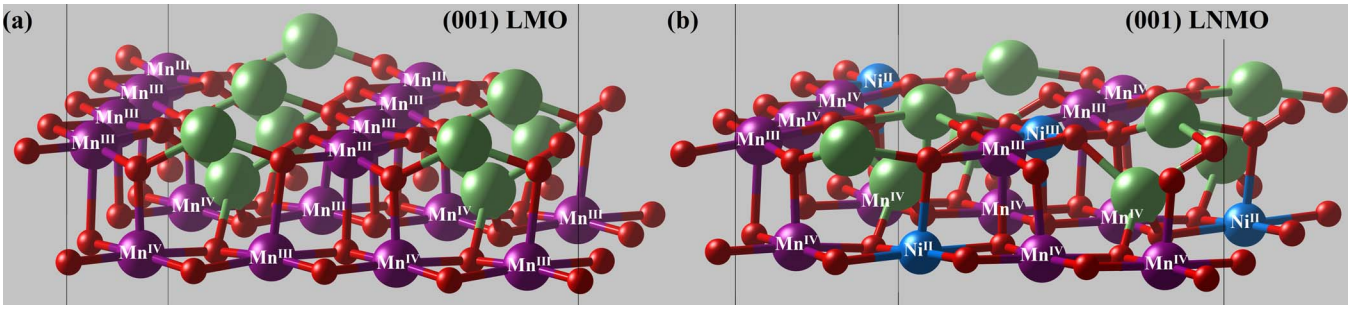


**Figure 2.** Distributions of transition-metal oxidation states on the fully lithiated (001) LMO and LNMO surfaces. Li, Ni, Mn and O atoms are depicted in green, blue, purple, and red, respectively.

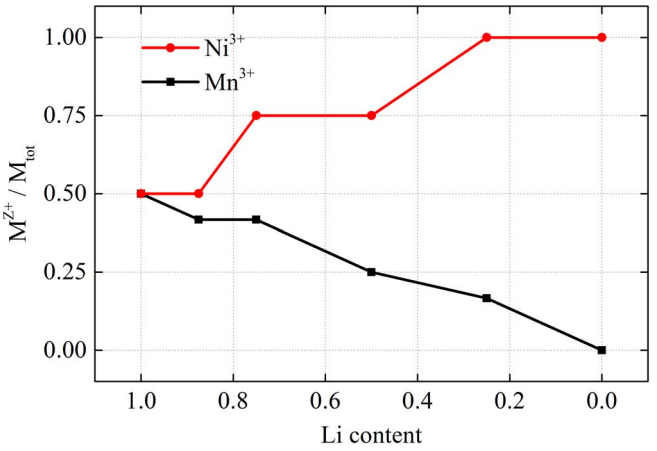


**Figure 3.** The fraction of the uppermost surface Ni(III) and Mn(III) ions with respect to the total number of surface Ni (Ni(II) + Ni(III)) and Mn (Mn(III) + Mn(IV)) ions for the (001) LNMO surface as a function of surface lithiation state. Li content of 1.0 and 0.0 denote fully lithiated and surface delithiated systems, respectively.

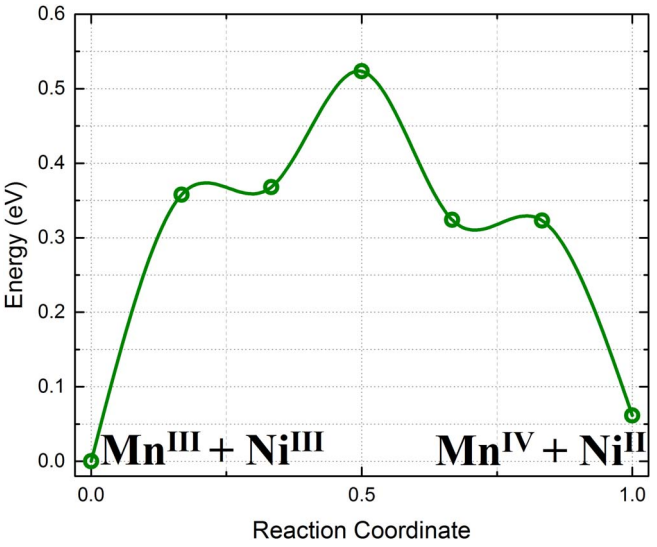


**Figure 4.** Energy profile for the Ni/Mn disproportionation reaction at the lithiated (001) LNMO surface obtained through CI-NEB calculations.

oxidation states for both Ni and Mn can be observed on the (001) surface depending on state of charge (lithiation) as demonstrated in Figure 3. For the first-layer delithiated MnO-terminated surface, however, we observe only Ni(III) and Mn(IV) ions, while Ni(II) ions are all in the bulk of the slab.

To gain more insights into the interplay between various oxidation states on (001) LNMO, we perform CI-NEB simulations for the following transition-metal charge transfer reaction:

$$Ni(II) + Mn(IV) \rightarrow Ni(III) + Mn(III) \quad [1]$$

For the fully lithiated (001) LNMO surface where all four transition-metal cations are observed, CI-NEB calculations show that conversion of one surface Ni(III) + Mn(III) pair into Ni(II) + Mn(IV) destabilizes the system by 0.06 eV with an activation barrier for electron transfer of about 0.52 eV (see Figure 4). The energy difference between these two states becomes negligible when half of the surface is delithiated with a similar activation barrier. Overall, our simulations show that for the fully lithiated (001) surface the configuration with 1:1 ratio of Ni(II)/Ni(III) and Mn(III)/Mn(IV) is slightly more stable than the surface with only one valence state for each transition metal on the surface. Such small energy differences between various configurations, however, should affect the calculated (001) surface energy only negligibly. A mixture of all four cations on the (001) surface should also be entropically favored at elevated temperatures which is observed in our AIMD simulations. The properties of the (111)

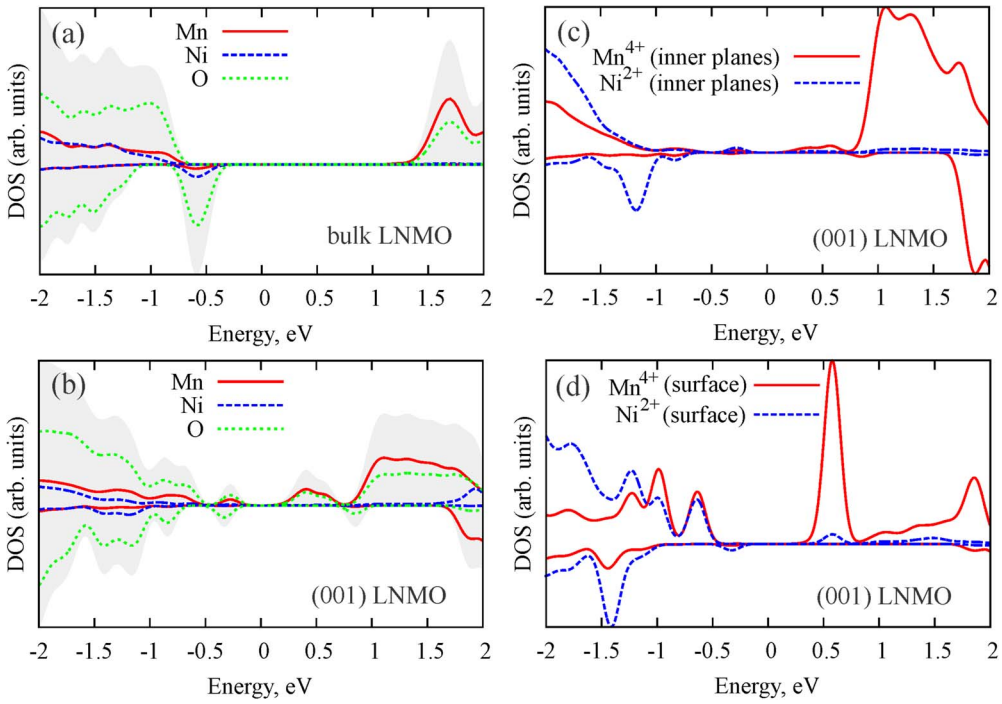


**Figure 5.** Total (grey area) and projected density of states (PDOS) calculated for bulk (a) and (001) surface slab (b-d) LNMO, (b) depicts DOS projected onto all Mn, Ni and O atoms of the slab, (c) - onto Mn(IV)and Ni(II) from the interior of the slab, and (d) - onto Mn(IV) and Ni(II) from the terminating surfaces of the slab.

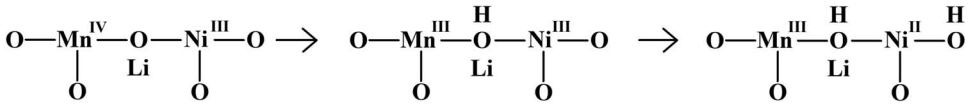

**Figure 6.** Schematic showing the result of successive protonation of surface oxygen atoms on transition-metal oxidation states at the (001) LNMO surface.

surface where all surface transition metals are fully coordinated by O atoms are similar to the LNMO bulk where only Ni(II) + Mn(IV) are energetically stable. The oxidation states of both Mn and Ni from the (111) LNMO surface that are substituted through surface reconstruction into tetrahedral sites in bulk are of Mn(II) and Ni(II).

We also analyze the electronic structure of bulk and surface LNMO based on the calculated projected density of states (PDOS) shown in Figure 5. It is seen that the in-gap states are induced by the uppermost surface Mn and Ni atoms. Moreover, PDOS obtained for the fully lithiated (001) LNMO surface demonstrates that the Ni(II) and Mn(IV) bands do overlap (Figure 5d) which makes their conversion to Ni(III) and Mn(III) on the surface favorable, whereas the Ni(II) and Mn(IV) bands coming from the bulk species of the slab are similar to the LNMO bulk case thus disfavoring changes in oxidation states to Ni(III) and Mn(III).

Since it is well established that the presence of trace amounts of acid in the electrolyte can lead to a more pronounced transition-metal dissolution in spinel oxides, we also analyze how protonation of surface oxygen atoms affects Ni and Mn oxidation states. In general, we find that surface protonation results in lowering the oxidation states of surface Mn and Ni cations with Mn displaying a larger propensity to be reduced. In the example of the first-layer delithiated (001) LNMO surface, where the oxidation states of Mn and Ni on the surface are Mn(IV) and Ni(III) only, protonation of the first surface oxygen atom that bridges Ni(III) and Mn(IV) leads to the reduction of Mn(IV) to Mn(III) (Figure 6). Through successive protonation of the second surface oxygen atom, reduction of the Ni ion from Ni(III) to Ni(II) is observed. The reduction from Mn(IV) to Mn(III) and from Ni(III) to Ni(II) is identified by the increase in magnetic moments from 3.2 $\mu_B$ to 3.8 $\mu_B$ for Mn and from 0.9 $\mu_B$ to 1.6 $\mu_B$ for Ni case. Such reduction of Mn and Ni ions also results in the M−O bond weakening where the M-O bonds elongate by about 0.1 Å on average.

It is also known that the presence of oxygen vacancies may influence the valence state of transition metals in spinel oxides. Based on our systematic calculations, it is found that for the first-layer delithiated (001) facet the lowest energy site is when the oxygen vacancy forms the bonds with Ni, Mn and Li ions, as shown in Figure 7, which reduce Mn(IV) to Mn(III) and Ni(III) to Ni(II). For the (111) surface we find that the oxygen vacancy prefers to bind to Ni(II) and two Mn(IV) ions and reduce both Mn to Mn(III). This is in general agreement with the finding for bulk LNMO where it was demonstrated that oxygen vacancy preferentially binds to one or two neighboring Ni ions and also converts Mn(IV) nearest to the vacancy to Mn(III).[45] Similarly, we find that surface Mn(III) in the LMO spinel are reduced to Mn(II) by the nearest-neighbor oxygen vacancies.

Our study thus suggests that both protonation and formation of oxygen vacancies on the (001) spinel surface can lead to the changes in oxidation states of transition metals by promoting transition metal reduction. In relation to transition-metal dissolution, however, our results do not allow us to explain experimental findings as to why the amount of dissolved transition metals from LNMO increases at the charged state, not the discharged state.[13,18] This is partly because under real battery operation conditions, the concentration of transition metals in various oxidation states on the surface should also depend on several factors such as the concentration of oxygen vacancies, the extent of surface protonation, adsorption of electrolyte species and how these factors affect transition-metal dissolution mechanism and kinetics.

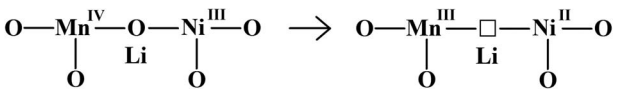

**Figure 7.** Effect of the presence of a single oxygen vacancy at the (001) LNMO surface on Mn and Ni oxidation states.

## Conclusions

By employing a series of DFT calculations augmented by AIMD simulations, we examined stability of various oxidation states for both Mn and Ni at the (001) and (111) surfaces of LMO and LNMO spinel oxides. It was found that the charge transfer between Ni and Mn at the (001) LNMO surface plays an important role in lowering the oxidation state of surface Mn at the fully discharged (lithiated) state where Mn and Ni exhibit mixed Mn(III)/Mn(IV) and Ni(II)/Ni(III) oxidation states on the surface. This is, however, not the case for the partially delithiated (001) surface where only Ni(III) and Mn(IV) can be observed on the surface. Both protonation of surface oxygen atoms and presence of oxygen vacancies are found to contribute to the reduction of surface transition metals. In contrast, the (111) LNMO surface characterized by full coordination of surface transition metals with oxygen atoms is determined to behave similarly to the bulk material and should be much less prone to Mn and Ni dissolution.

## Acknowledgments

This work was supported by the startup package provided by the University of Nebraska-Lincoln. This research used resources of the National Energy Research Scientific Computing Center, a DOE Office of Science User Facility supported by the Office of Science of the U.S. Department of Energy under Contract No. DE-AC02-05CH11231, and the Holland Supercomputing Center at the University of Nebraska-Lincoln.

## ORCID

Nadia N. Intan https://orcid.org/0000-0003-1967-178X
Konstantin Klyukin https://orcid.org/0000-0001-8325-8725
Vitaly Alexandrov https://orcid.org/0000-0003-2063-6914

## References

1. M. Thackeray, W. David, P. Bruce, and J. Goodenough, *Mater. Res. Bull.*, **18**, 461 (1983).
2. M. Thackeray, P. Johnson, L. De Picciotto, P. Bruce, and J. Goodenough, *Mater. Res. Bull.*, **19**, 179 (1984).
3. A. Kraytsberg and Y. Ein-Eli, *Adv. Energy Mater.*, **2**, 922 (2012).
4. M. Hu, X. Pang, and Z. Zhou, *J. Power Sources*, **237**, 229 (2013).
5. J. Tarascon and D. Guyomard, *J. Electrochem. Soc.*, **138**, 2864 (1991).
6. W. Choi and A. Manthiram, *J. Electrochem. Soc.*, **153**, A1760 (2006).
7. G. Liu, L. Wen, and Y. Liu, *J. Solid State Electrochem.*, **14**, 2191 (2010).
8. Q. Zhong, A. Bonakdarpour, M. Zhang, Y. Gao, and J. Dahn, *J. Electrochem. Soc.*, **144**, 205 (1997).
9. Y. Terada, K. Yasaka, F. Nishikawa, T. Konishi, M. Yoshio, and I. Nakai, *J. Solid State Chem.*, **156**, 286 (2001).
10. M.-C. Yang, B. Xu, J.-H. Cheng, C.-J. Pan, B.-J. Hwang, and Y. S. Meng, *Chem. Mater.*, **23**, 2832 (2011).
11. J. Ma, P. Hu, G. Cui, and L. Chen, *Chem. Mater.*, **28**, 3578 (2016).
12. X. Xiao, D. Ahn, Z. Liu, J.-H. Kim, and P. Lu, *Electrochem. Commun.*, **32**, 31 (2013).
13. N. P. W. Pieczonka, Z. Liu, P. Lu, K. L. Olson, J. Moote, B. R. Powell, and J.-H. Kim, *J. Phys. Chem. C*, **117**, 15947 (2013).
14. N. S. Norberg, S. F. Lux, and R. Kostecki, *Electrochem. Commun.*, **34**, 29 (2013).
15. N. Kumar, K. Leung, and D. J. Siegel, *J. Electrochem. Soc.*, **161**, E3059 (2016).
16. K. Leung, *Chem. Mater.*, **29**, 2550 (2016).
17. H. Yu, Y. Qian, M. Otaru, D. Tang, S. Guo, Y. Zhu, and H. Zhou, *Energy Environ. Sci.*, **7**, 1068 (2014).

18. R. Qiao, Y. Wang, P. Olalde-Velasco, H. Li, Y.-S. Hu, and W. Yang, *J. Power Sources*, **273**, 1120 (2015).
19. I. Taniguchi, C. Lim, D. Song, and M. Wakihara, *Solid State Ionics*, **146**, 239 (2002).
20. K. Matsuda and I. Taniguchi, *J. Power Sources*, **132**, 156 (2004).
21. A. Karim, S. Fosse, and K. A. Persson, *Phys. Rev. B: Condens. Matter*, **87**, 075322 (2013).
22. S. Kim, M. Aykol, and C. Wolverton, *Phys. Rev. B: Condens. Matter*, **92**, 115411 (2015).
23. E. Lee and K. A. Persson, *Nanotechnology*, **24**, 424007 (2013).
24. E. Lee and K. A. Persson, *Nanotechnology*, **25**, 159501 (2014).
25. J. Shi, Z. Wang, and Y. Fu, *J. Mater. Sci.*, **52**, 605 (2017).
26. R. Benedek and M. Thackeray, *Phys. Rev. B: Condens. Matter*, **83**, 195439 (2011).
27. R. Benedek, *J. Phys. Chem. C*, **121**, 22049 (2017).
28. K. Leung, *J. Phys. Chem. C*, **116**, 9852 (2012).
29. G. Kresse and J. Furthmüller, *Comput. Mater. Sci.*, **6**, 15 (1996).
30. G. Kresse and J. Furthmüller, *Phys. Rev. B: Condens. Matter*, **54**, 11169 (1996).
31. P. E. Blöchl, *Phys. Rev. B: Condens. Matter*, **50**, 17953 (1994).
32. J. P. Perdew, K. Burke, and M. Ernzerhof, *Phys. Rev. Lett.*, **78**, 1396 (1997).
33. J. P. Perdew, A. Ruzsinszky, G. I. Csonka, O. A. Vydrov, G. E. Scuseria, L. A. Constantin, X. Zhou, and K. Burke, *Phys. Rev. Lett.*, **100**, 136406 (2008).
34. A. Jain, G. Hautier, S. P. Ong, C. J. Moore, C. C. Fischer, K. A. Persson, and G. Ceder, *Phys. Rev. B: Condens. Matter*, **84**, 045115 (2011).
35. T. Mueller, G. Hautier, A. Jain, and G. Ceder, *Chem. Mater.*, **23**, 3854 (2011).
36. G. Hautier, S. P. Ong, A. Jain, C. J. Moore, and G. Ceder, *Phys. Rev. B: Condens. Matter*, **85**, 155208 (2012).
37. T.-F. Yi, Y. Xie, M.-F. Ye, L.-J. Jiang, R.-S. Zhu, and Y.-R. Zhu, *Ionics*, **17**, 383 (2011).
38. A. Manthiram, K. Chemelewski, and E.-S. Lee, *Energy Environ. Sci.*, **7**, 1339 (2014).
39. Y. Chen, Y. Sun, and X. Huang, *Comput. Mater. Sci.*, **115**, 109 (2016).
40. H. J. Monkhorst and J. D. Pack, *Phys. Rev. B: Condens. Matter*, **13**, 5188 (1976).
41. N. Bišķup, J. Martínez, M. Arroyo y de Dompablo, P. Díaz-Carrasco, and J. Morales, *J. Appl. Phys.*, **100**, 093908 (2006).
42. N. Amdouni, K. Zaghib, F. Gendron, A. Mauger, and C. Julien, *J. Magn. Magn. Mater.*, **309**, 100 (2007).
43. G. Henkelman, B. P. Uberuaga, and H. Jónsson, *J. Chem. Phys.*, **113**, 9901 (2000).
44. C. Ouyang, Y. Du, S. Shi, and M. Lei, *Phys. Lett. A*, **373**, 2796 (2009).
45. P. V. Sushko, K. M. Rosso, J.-G. Zhang, J. Liu, and M. L. Sushko, *Adv. Funct. Mater.*, **23**, 5530 (2013).